frontiers | Frontiers in Physics

TYPE Original Research
PUBLISHED 20 December 2022
DOI 10.3389/fphy.2022.1093284

OPEN ACCESS

EDITED BY
Cong Liu,
Nokia Bell Labs, United States

REVIEWED BY
Weijun Luo,
Boston University, United States
Jun Zhu,
Guangxi Normal University, China

*CORRESPONDENCE
Shuyan Zhang,
zhang_shuyan@ibb.a-star.edu.sg
Malini Olivo,
malini_olivo@ibb.a-star.edu.sg

SPECIALTY SECTION
This article was submitted to Optics and Photonics,
a section of the journal
Frontiers in Physics

RECEIVED 08 November 2022
ACCEPTED 07 December 2022
PUBLISHED 20 December 2022

CITATION
Zhang S, Bi R, Zhang R, Qi Y, Salim RBSM and Olivo M (2022), An all metasurface-based fiber needle probe for Raman spectroscopy.
Front. Phys. 10:1093284.
doi: 10.3389/fphy.2022.1093284

An all metasurface-based fiber needle probe for Raman spectroscopy

Shuyan Zhang[1]*, Renzhe Bi[1], Ruochong Zhang[1], Yi Qi[1], Rasyiqah Bte Shaik Mohamed Salim[1,2] and Malini Olivo[1]*

[1]Translational Biophotonics Laboratory, Institute of Bioengineering and Bioimaging, A*STAR, Singapore, Singapore, [2]Department of Biomedical Engineering, National University of Singapore, Singapore, Singapore

Optical fiber-based spectroscopy sensors are widely used for industrial and biomedical applications. They normally consist of at least one excitation fiber and one collection fiber. However, the excitation and collection fibers are placed side by side, so the focal spots do not coincide. In addition, Raman probes whose excitation and emission span a wide wavelength range are limited by wavelength-dependent focal length variation, low sensitivity, and bulky size impeding their clinical adoption. To overcome the challenges, we propose an all metasurface integrated fiber solution. The metasurface technology is well suited for this application because it relies on specially designed nanostructures to manipulate light properties in an ultrathin footprint. Here we used our earlier demonstrated dual-wavelength excitation Raman probe as an example. The two excitation fibers at 671 nm and 785 nm feature a hybrid metasurface lens (metalens) including a narrow band pass filter and an off-axis focusing metalens. The collection fiber at 810—910 nm features an achromatic broadband on-axis focusing metalens. Simulation results show that by integrating the metalenses, the focal spots of the excitation beams and the collection beam coincide with a beam size of 4.6 μm, 4.6 μm, and 11.3 μm in the x-, y-, and z-axis, respectively. Moreover, the probe size shrinks by 100 times and becomes a needle probe. The needle probe will enable new applications such as small animal *in vivo* experiments, medical endoscopy experiments, and neonatal skin analysis for hard-to-reach areas. Furthermore, the proposed solution can be applied to work with any optical fiber-based spectroscopy sensors because the designs can be readily fabricated and put into practical use.

KEYWORDS

metasurface, fiber, Raman spectroscopy, biosensing, achromatic

1 Introduction

Raman spectroscopy is widely used for biomedical applications such as skin analysis and early cancer detection [1–9]. Recently there has been a lot of development in miniaturizing Raman spectroscopy-based devices for *in vivo* studies [10–12]. We have earlier reported a handheld portable Raman spectroscopy device for skin analysis [13].

The confocal configuration allowed data collection at different dermal layers in a less invasive manner compared to the conventional *ex vivo* tape stripping method. The dual-wavelength excitation configuration allowed an ultrawide band characterization of the stratum corneum thickness, natural moisturizing factor, and water content. The scanning time was about 2 min for 10 depths reducing 50% of time compared to a commercial Raman spectroscopy system. However, there are several limitations. The first is that the dual-wavelength excitation was sequential by using a fiber array multiplexing module. A simultaneous excitation would be ideal so that different biological features can be measured at the same time. The second is that the excitation and collection beam spots were not focused at the same spot on the sample because the excitation and collection fibers were put side by side and the wavelengths were different. This limitation is a common issue faced by many fiber-based endoscopic probes [12, 14–17]. A coincidence of the beam spots would be ideal to achieve the best spatial resolution. The third is that the overall handheld probe size was on the order of hundreds of millimeters. Although it has already been miniaturized from a benchtop device to a portable handheld device, a further size reduction would enable the device to perform measurements for hard-to-reach areas and endoscopic applications. It is worth mentioning that the limitations mentioned above may also be experienced by non-Raman spectroscopy-based fiber sensors.

The metasurface technology is a rising star in the nanophotonics field and is explored here to address these limitations. It is based on specially designed nanostructures that allow manipulation of the light properties, such as phase and amplitude of the transmitted, reflected, or scattered light, at a sub-wavelength scale. It provides the potential to redesign conventional refractive optics-based optical components in an ultrathin footprint (approximately 10^3 times thinner) and achieve new functionalities that never existed before. Over the last decade, research groups worldwide have demonstrated metasurface-based optical components with superior performance to conventional optical components, such as combining multiple functions in a single flat optics device and correcting aberrations to achieve diffraction-limited focusing [18–26]. The concept has started attracting attention in biomedical imaging and sensing too [27, 28]. Pahlevaninezhad et al. implemented the concept of bijective illumination collection imaging for optical coherence tomography of tissues [29]. It was realized through the use of two metasurface lenses (metalens), each bent the incident light at an angle and focused it into a line for the excitation path and the collection path, respectively. The excitation and collection spots coincided and a lateral resolution of 3.2 μm over a depth of 1.25 mm was achieved at a wavelength of 1.3 μm. Beyond single-wavelength metalenses, recent research has shown the merits of broadband achromatic metalenses. Chen et al. has designed broadband achromatic metalens for focusing and imaging in the visible range between 470 and 670 nm [30]. This was achieved by controlling the phase, group delay, and group delay dispersion of the metalens using TiO_2 nanofins of differing widths and lengths and height 600 nm. Wang et al. has demonstrated a broadband achromatic metalens for imaging in the near-infrared (NIR) range 650–1000 nm [31]. The authors achieved high efficiency with an impressive TiO_2 nanopillar height of 1500 nm and 90° vertical side walls.

Inspired by the previous work, we designed and simulated five different metasurface components that can be integrated on the fiber facets to replace the optical filters and lenses in the current handheld confocal dual-wavelength Raman spectroscopy device. Specifically, this all-metasurface design includes two narrow band pass filters and two off-axis focusing metalenses allowing for simultaneous excitation of two beams at 671 nm and 785 nm and one broadband achromatic on-axis focusing metalens from 810 nm to 910 nm for the collection beam. The focal spots of the excitation beams and collection beam completely overlap so the optimum lateral and axial resolutions were achieved. The new design reduced the overall probe size by approximately 100 times, from 200 mm to 2 mm in diameter into a needle size. We made sure that the design could be fabricated and put into practical use. The parameters of the metasurface nanostructures were based on literature-reported fabricated devices and all metasurfaces have achieved high efficiency of 70% across the entire wavelength range of interest. The methodology and results presented here not only help resolve the limitations of our current probe design, but also extend the confocal Raman spectroscopy applications to oral cavity examinations [32], small animal experiments [14], medical endoscopic experiments [33], and neonatal or infant skin analysis for hard-to-reach areas [34], as shown in Figure 1.

2 Methodology

Figure 2 gives an overview of the design methodology. Figure 2A shows a schematic of the probe head made of three optical fibers including two excitation fibers on the side, one collection fiber in the middle, and five metasurface devices at the distal end of the fiber facets, labeled as (1)–(5). The excitation fibers are large-mode area single-mode photonic crystal fibers with a core diameter of 20 μm and a wavelength range of 600–1700 nm (LMA-20, Thorlabs). The collection fiber has a core diameter of 25 μm and a wavelength range of 800–1700 nm (LMA-25, Thorlabs). Single-mode fibers were used because metasurface works only with single-mode incident beams. However, traditional single-mode fibers have a small core diameter of 5 μm and a narrower wavelength range. To maximize the interaction of the light and metasurfaces at the fiber facets, photonic crystal fibers with large mode areas are needed. Our new metasurface-based designs were based on commercially available large mode area single-mode photonic crystal fibers, but it has been shown in the literature that the

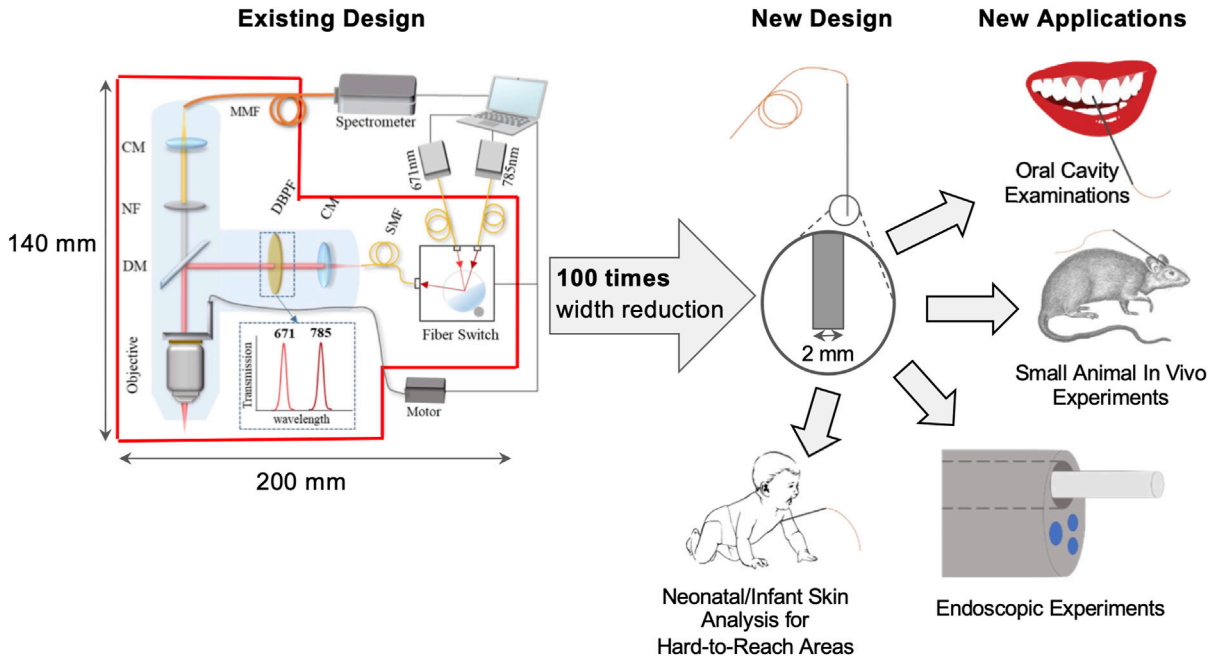

FIGURE 1
Overview of existing and new design of Raman probe. Schematics of existing and new probes and potential applications of the new design.

mode area can be as large as 100 μm [35]. The collection fiber has a low cut-off wavelength at 800 nm so that any excitation light at shorter wavelengths will be blocked. The five metasurfaces in our design include 1) 671 nm narrow band pass filter (NBPF), 2) 671 nm off-axis focusing metalens, 3) 785 nm narrow band pass filter, 4) 785 nm off-axis focusing metalens, and 5) 810–910 nm broadband achromatic on-axis focusing metalens. Metasurface 1)–4) were designed to replace all the optical components in the excitation beam path in the earlier design [13], i.e., metasurface 1) and 3) for the dual-passband laser cleaning filters and metasurface 2) and 4) for the fiber array multiplexing module, the collimator, and the objective. Metasurface 5) was designed to replace the optical components in the collection beam path including the objective, the notch filter, and the collimator.

Figure 2B summarizes the design parameters for the three metalenses, i.e., 2), 4), and 5). The diameters of the metalenses were calculated based on the core diameters of the photonic crystal fibers and their divergence due to the metalens thickness and NBPF thickness. The diameters were 45.9 μm, 51.1 μm, and 51.8 μm for metalens 2), 4), and 5), respectively. The focal lengths were calculated along the beam path. The focal lengths were 356.9 μm, 356.9 μm, and 260.4 μm. The focusing angles were calculated based on the equation, $\theta = cos^{-1}\left(f_{on-axis}/f_{off-axis}\right)$, where f is the focal length. The focusing angles were 43.1°, −43.1°, and 0. The numerical apertures (NA) were calculated based on the equation, $NA = sin[tan^{-1}(D/2f)]$, where D is the diameter. The NAs were 0.06, 0.07, and 0.10. It is noted that although the NAs are small, the focusing angles for the off-axis metalenses are large which adds challenges to the metalens design.

Figure 2C is the schematic of the NBPF metasurface and off-axis metalens combined structure for the excitation fiber. The substrate side will be attached to the fiber facet. The output light from the fiber will first pass through the substrate (SiO_2), then the NBPF layers (Ag/Poly (methyl methacrylate) or PMMA/Ag), and finally the metalens (TiO_2). The optical properties of TiO_2 could be found in the supplementary information. The purpose of the NBPF was to only pass through the excitation wavelengths and filter out the autofluorescence signals generated from the optical fibers. The NBPF was a Fabry-Pérot cavity consisting of the PMMA material sandwiched by two Ag mirrors, which allowed only optical waves in resonance to pass through. The bandwidth of the transmission peaks (i.e., linewidth) and the free spectral range between each transmission peak (i.e., finesse) can be adjusted by the cavity length, the material of the cavity, and the thickness of the cavity. The metalens on top of the NBPF focuses incoming light at an angle. The metalens was made of TiO_2 circular pillars. The parameters of the unit cell design were height = 1500 nm, diameter = 50–130 nm (for λ = 671 nm) and 50 to 170 (for λ = 785 nm), and period = 160 nm (for λ = 671 nm) and 200 nm (for λ = 785 nm). The phase maps and transmission maps are presented in the supplementary information, see Supplementary Figure S1. The phase coverage was 2π and the transmission was close to 1. Note that all the design parameters

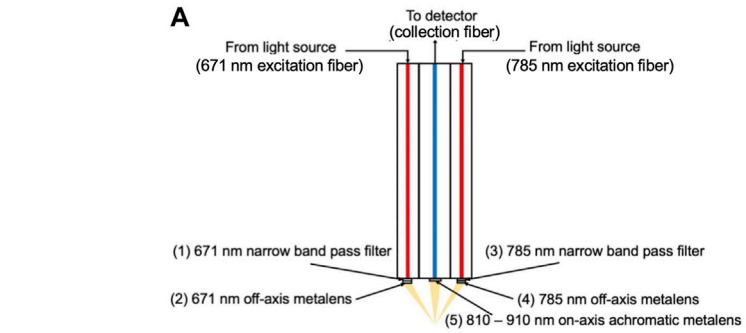

B

	671 nm off-axis	785 nm off-axis	810 - 910 nm achromatic on-axis
Diameter	45.9 μm	51.1 μm	51.8 μm
Focal Length	356.9 μm	356.9 μm	260.4 μm
Focusing Angle	43.1°	-43.1°	0
NA	0.06	0.07	0.10

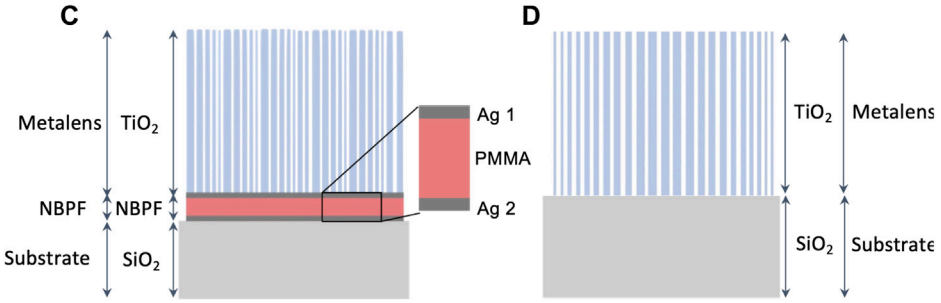

FIGURE 2
Schematic of new Raman probe and metasurfaces. **(A)** Schematic of new Raman probe, which consists of two excitation fibers (671 and 785 nm), one collection fiber, as well as five metasurfaces—1) 671 nm narrow band pass filter (NBPF), 2) 671 nm off-axis metalens, 3) 785 nm NBPF, 4) 785 nm off-axis metalens, 5) 810–910 nm on-axis achromatic metalens. **(B)** Specifications of metalenses—Diameter, Focal Length, and Numerical Aperture (NA). **(C)** Schematic of off-axis metalens and NBPF—consisting of the SiO_2 substrate, NBPF, and off-axis metalens comprising of TiO_2 nanopillars and a SiO_2 layer. **(D)** Schematic of on-axis achromatic metalens—consisting of the SiO_2 substrate and the achromatic metalens which is made up of TiO_2 nanopillars.

were proved to be fabricatable by literature [30, 36]. The design equation for the off-axis focusing function can be found in [37], where each metalens element at position (x, y) needs to provide a phase shift φ that satisfies:

$$\varphi = -\frac{2\pi}{\lambda}\left[\sqrt{\left(x - x_f\right)^2 + \left(y - y_f\right)^2 + \left(z_f\right)^2} - f\right] \quad (1)$$

where $f = \sqrt{x_f^2 + y_f^2 + z_f^2}$ is the focal length from the center of the metalens to the focal point at the position (x_f, y_f).

Figure 2D is the schematic of the broadband achromatic on-axis metalens for the collection fiber. The substrate material was SiO_2 and the metalens material was TiO_2. Based on the design principles described in [30] for a metalens to focus achromatically, not only the phase shift at each position needs to be satisfied, but also the group delay. Therefore, we simulated a pool of pillars with different shapes and sizes including a circular, cross, and square shape, as shown in Figure 3A. These shapes are symmetrical, so the design is independent of the polarization of the incident light. The height of the nanopillars was 1500 nm which was much higher than the off-axis design because the increased height will increase the group delay coverage of the unit cells [31]. The diameters and lengths were 50–200 nm for all three shapes. For on-axis focusing, the phase equation follows Eq. 1 by setting $x_f = y_f = 0$, $f = z_f$, and $\lambda = \lambda_{center} = 860\,nm$. The group delay equation is the first derivative of the phase equation with respect to the wavelength at $\lambda_{center} = 860\,nm$. Figure 3B shows the required group delay in femtosecond versus phase in radians for the metalens and the satisfied circular, cross, and square unit cells. The selection of unit cells was based on the principle of minimum sum of squared residuals. Figures 3C, D are the actual phase and group delay realized by the selected unit cells as a function of radial positions of the metalens, respectively.

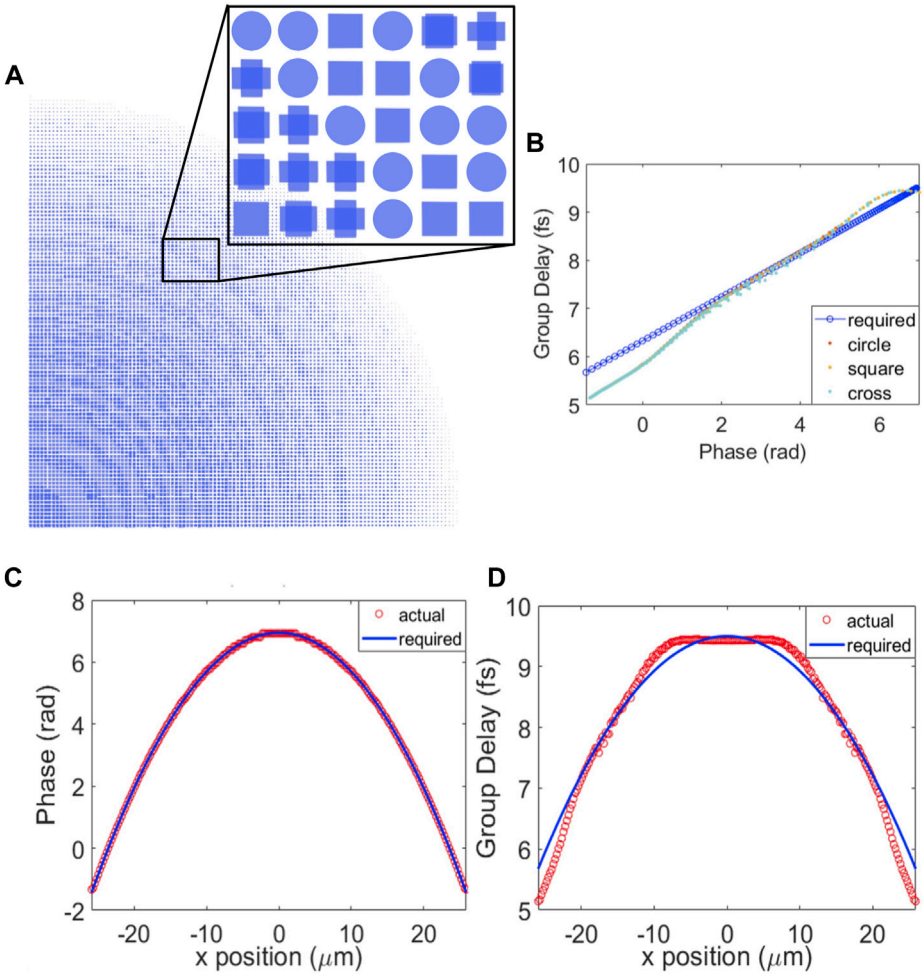

FIGURE 3
Design for 810–910 nm achromatic on-axis metalens. **(A)** Top view of the upper right quarter of achromatic metalens and cross-sections of nanopillars. **(B)** Group delay vs. phase plot for achromatic metalens - Required group delay vs. phase for each radial position and simulated group delay and phase for nanopillar unit cells. **(C)** Phase vs. x position plot—Actual phase value of selected nanopillar and required phase value at each x position. **(D)** Group delay vs. x position plot—Actual group delay value of selected nanopillar and required group delay value at each x position.

The phase was matched perfectly, and the group delay was matched well. The discrepancy was due to insufficient group delay coverage. This can be improved by having a larger pillar height and a smaller pillar size, but the fabrication of such high aspect ratio pillars will be challenging. Here, the design parameters have been demonstrated on fabricated devices in [31]. Non-etheless, the current parameters are satisfactory to achieve desirable metalens performance which will be discussed in Section 3.

All simulations were performed using commercial FDTD software (Lumerical, Ansys Inc.). For the metasurface designs of the excitation beams, the mesh setting was auto-nonuniform with accuracy 1 and the boundary conditions were PML (stretched coordinate PML) in x-axis, Symmetric in y-axis, and PML in z-axis. For metasurface designs of the collection beam, the mesh setting was auto-nonuniform with accuracy 3 and the boundary conditions were Anti-symmetric in x-axis, Symmetric in y-axis, and PML in z-axis.

3 Results and discussion

This section discusses the simulated results of five metasurfaces mentioned in the last section. It was divided into three subsections, one for the 671 nm excitation fiber, one for the 785 nm excitation fiber, and the last one for the 810–910 nm collection fiber.

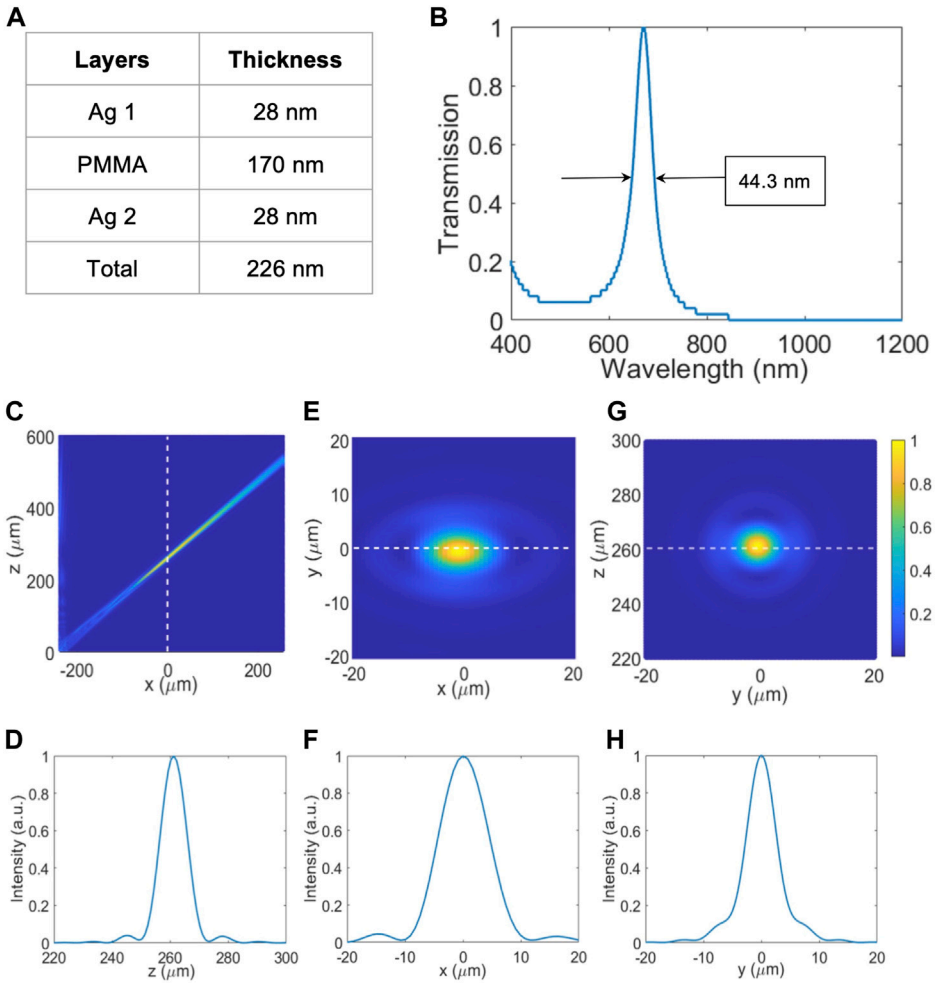

FIGURE 4
Simulation results for 671 nm NBPF and off-axis metalens. **(A)** Table consolidating the thickness of each NBPF layer and its material. **(B)** Transmission vs. Wavelength plot of 671 nm NBPF for the range of 400–1200 nm with peak wavelength = 670.6 nm and FWHM = 44.3 nm. **(C)** Normalized intensity plot of the focal point profile of 671 nm off-axis focusing on the x-z plane. **(D)** Normalized intensity plot of the focal point along the z-axis. **(E)** Normalized Intensity plot of focal point profile of 671 nm off-axis focusing on the x-y plane. **(F)** Normalized intensity plot of the focal point along the x-axis. **(G)** Normalized Intensity plot of focal point profile of 671 nm off-axis focusing on the y-z plane. **(H)** Normalized intensity plot of the focal point along the y-axis.

3.1 Metasurfaces for 671 nm excitation fiber

It consisted of a hybrid design of an NBPF and a metalens. Figure 4A summarizes the optimized parameters for the NBPF design. The total thickness was 226 nm including the two Ag mirror layers which were 28 nm thick each and the PMMA layer which was 170 nm thick. The optimization criteria were narrow transmission bandwidth, transmission peak position at the design wavelength, and high transmission efficiency. Figure 4B is the normalized transmission profile after the NBPF. The incident light was a plane wave with a wavelength range of 400–1200 nm. The bandwidth was measured by the full width at half maximum (FWHM) which was 44.3 nm. The transmission peak position was at 670.6 nm. The transmission efficiency was 64%. The loss came from metallic losses. It was observed that there was a loss of about 13% after passing through each Ag layer (see Supplementary Table S1). Figures 4C—H shows the electric field profiles of the output light after the NBPF and metalens at different plane cross sections. The NBPF and metalens were placed in the $x - y$ plane with the center at $x = -244.1\mu m$, $y = 0$. Figure 4C is the view of light propagation in the $x - z$ plane at $y = 0$. The output light after passing through the NBPF and metalens was focused off-axis at a deflection angle of −43.4° which was close to the designed angle. The distance between the position of the metalens center and the position with the highest intensity determines the off-axis focal length, $f_{off-axis} = 355.5\mu m$. The intensity profile (normalized) along

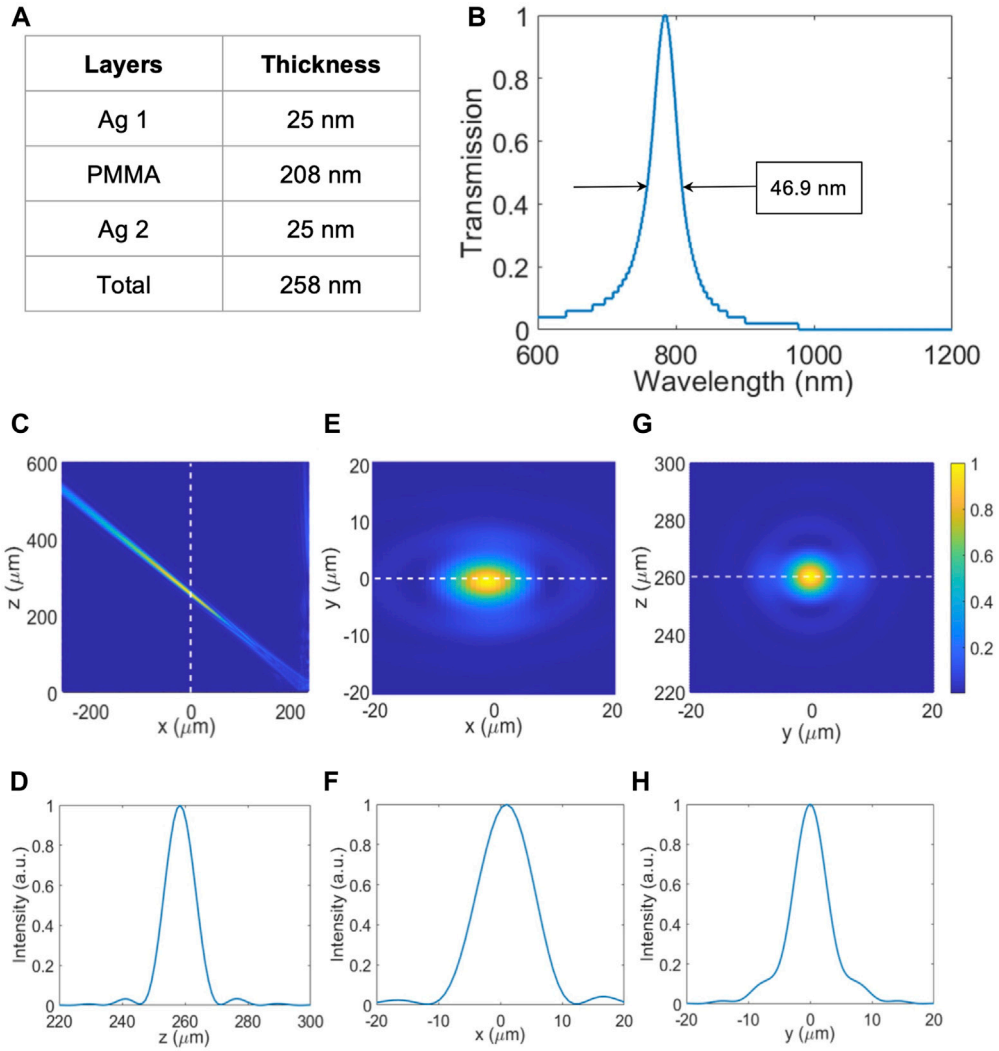

FIGURE 5
Simulation results for 785 nm NBPF and off-axis metalens. **(A)** Table consolidating the thickness of each NBPF layer and its material. **(B)** Transmission vs. Wavelength plot of 785 nm NBPF for the range of 600–1200 nm with the peak wavelength = 784.4 nm and FWHM = 46.9 nm. **(C)** Normalized intensity plot of the focal point profile of 785 nm off-axis focusing on the x-z plane. **(D)** Normalized intensity plot of the focal point along the z-axis. **(E)** Normalized intensity plot of the focal point profile of 785 nm off-axis focusing on the x-y plane. **(F)** Normalized intensity plot of the focal point along the x-axis. **(G)** Normalized intensity plot of the focal point profile of 785 nm off-axis focusing on the y-z plane. **(H)** Normalized intensity plot of the focal point along the y-axis.

the white dashed line at $x = 0$ is shown in Figure 4D. From the plot, the on-axis focal length could be determined, $f_{on-axis} = 258.4\,\mu m$. Figure 4E is the cross-sectional view of the focused beam profile in the $x - y$ plane at $z = f_{on-axis}$. Figure 4F is the intensity profile (normalized) along $y = 0$. From the plot, the FWHM of the focal profile can be determined, $FWHM_x = 9.7\,\mu m$. Figure 4G shows the focused beam profile in the $y - z$ plane at $x = 0$. Figure 4H is the intensity profile (normalized) along $z = f_{on-axis}$. From the plot, the FWHM of the focal profile can be determined, $FWHM_y = 5.9\,\mu m$. Note that $FWHM_x$ is slightly greater than $FWHM_y$, which is likely due to the off-axis focusing direction being set in the x direction. The overall transmission efficiency of the whole hybrid metalens design was 63%.

3.2 Metasurfaces for 785 nm excitation fiber

Similar to the 671 nm excitation fiber, the metasurfaces consisted of an NBPF design to only allow 785 nm wavelength to pass through and an off-axis metalens design to focus the

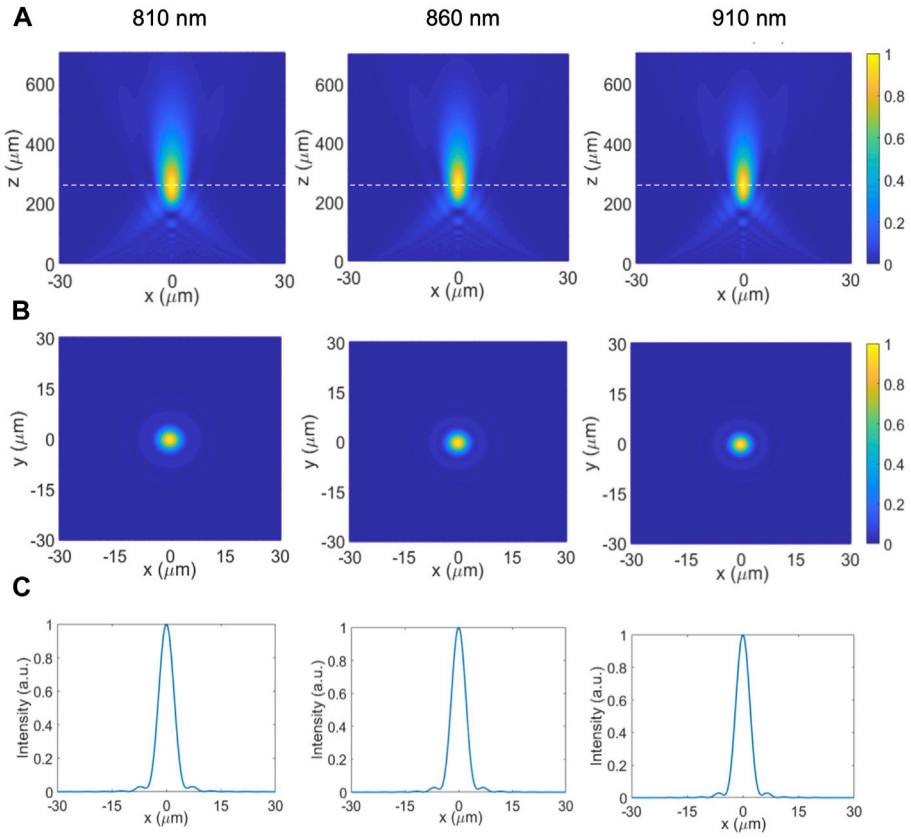

FIGURE 6
Simulation results for 810–910 nm achromatic on-axis metalens. **(A)** Normalized intensity plot of the focal point profile of achromatic metalens in the x-z plane at λ = 810, 860, and 910 nm. **(B)** Normalized intensity plot of the focal point profile of achromatic metalens in the x-y plane at λ = 810, 860, and 910 nm. **(C)** Normalized intensity plot of the focal point profile of achromatic metalens along the x-axis at λ = 810, 860, and 910 nm.

light at an angle so that the focal spot coincides with the focal spot of the 671 nm excitation fiber. Figure 5A shows the optimized values for the layer thicknesses of the NBPF structure. The thickness values of the Ag layers were 25 nm and the thickness of the PMMA layer was 208 nm making the total thickness of 258 nm. Figure 5B shows the optical performance of the NBPF where the FWHM was 46.9 nm, the peak position was at 784.4 nm, and the transmission efficiency was 66%. Figures 5C, E, G correspond to the normalized 2D electric field distributions of the metalens in the $x-z$ plane, $x-y$ plane, and $y-z$ plane, respectively. The metalens was placed in the $x-y$ plane with the center at $x = 244.1\,\mu m$, $y = 0$. The deflection angle and off-axis focal length were calculated from Figure 5C which were 43.4° and $f_{off-axis} = 355.5\,\mu m$. Figures 5D, F, H correspond to the normalized 1D electric field profiles of the metalens along the $z-axis$, $y-axis$, and $x-axis$, respectively. The on-axis focal length was calculated from Figure 5D which was $f_{on-axis} = 258.4\,\mu m$. The FWHMs of the focal spot were calculated from Figures 5F, H which were $FWHM_x = 10.4\,\mu m$ and $FWHM_y = 6.2\,\mu m$. The overall transmission efficiency after the metalens layer was 65%.

3.3 Metasurfaces for 810 nm–910 nm collection fiber

For biological analysis, the most commonly used Raman detection range is 810 nm–910 nm, hence the metalens at the facet of the collection fiber must maintain the same focal length in the entire wavelength range, i.e., broadband achromatic focusing. This is challenging because most metalenses are designed for a single wavelength and will experience chromatic aberration. In order to solve this challenge, both the required phase profile and the group delay profile need to be satisfied by the metalens nanostructures, as discussed in Section 2. The final result is presented in Figure 6. The metalens was placed in the $x-y$ plane with the center at $x = 0, y = 0, z = 0$. Figure 6A are the normalized 2D electric field distributions in the $x-z$ plane at $y = 0$ showing the light

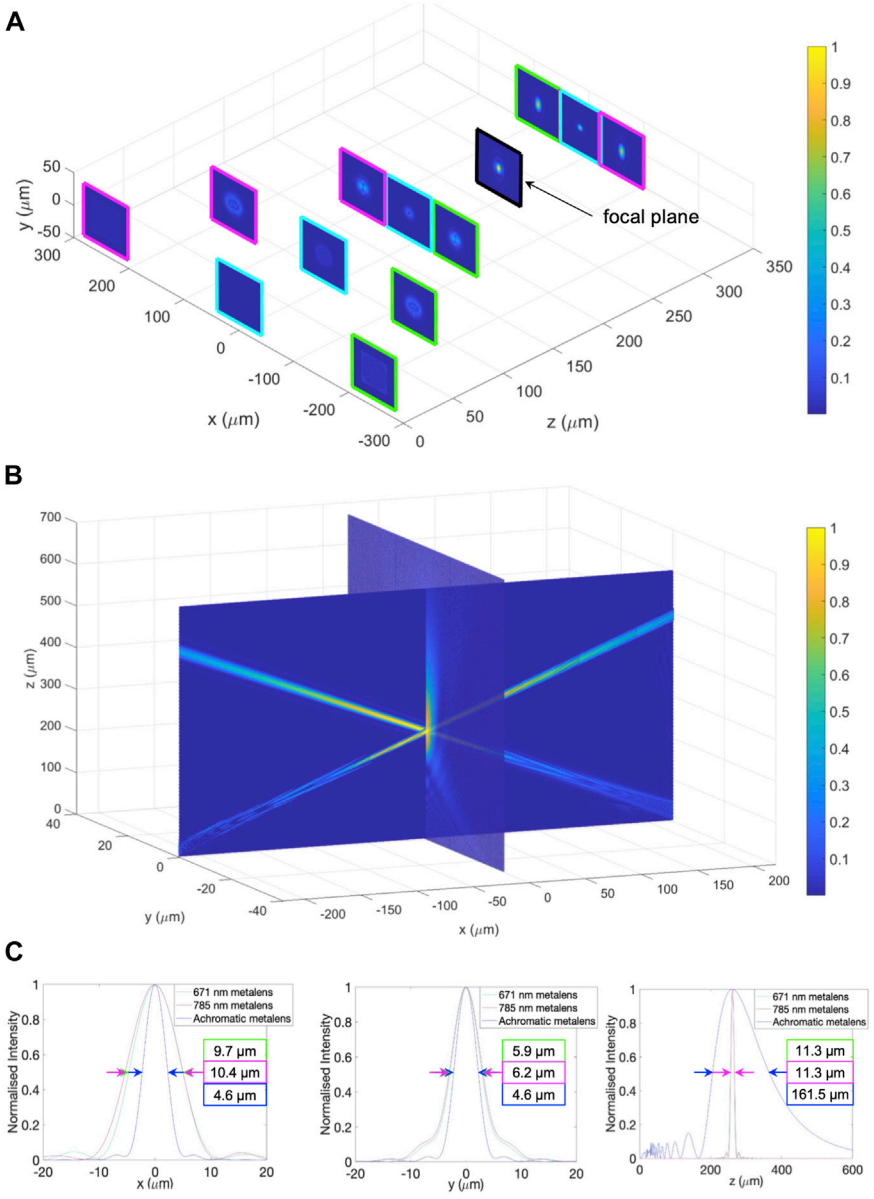

FIGURE 7
Focal point profiles of all metalenses. **(A)** 3D beam propagations of all three metalenses - magenta: 785 nm hybrid off-axis metalens, blue: 810–910 nm achromatic on-axis metalens, green: 671 nm hybrid off-axis metalens. The focal plane is shown in black. **(B)** Perspective view of the overlapping region of all three metalenses. **(C)** Normalized intensity plots of focal points along the x, y, and z-axis, showing the measurements of focal points in each direction.

propagation along the $z-axis$ at $\lambda = 810\,nm$, $860\,nm$, and $910\,nm$, respectively. The incident light constructively interfered at the focal point. The white dashed lines indicate the focus positions at the highest intensity points. The focal length is maintained across the entire wavelength range at $z = f = 260.5\,\mu m$. A more detailed plot containing the light propagation at 11 wavelengths can be found in the supplementary information (Supplementary Figure S2). The average transmission efficiency was 70%, among the highest for achromatic broadband metalenses in the NIR range reported in the literature. Figure 6B are the normalized 2D electric field distributions in the $x-y$ plane at $z = f$ showing the cross-sectional view of the focal spot. The field distributions were symmetrical in the x and y directions. Figure 6C is the normalized 1D electric field profile along the $x-axis$ (white dashed lines in Figure 6A) showing well-defined diffraction patterns. The simulated FWHM was 4.6 μm. The theoretical limit of FWHM at the central wavelength 860 nm is 3.2 μm. A

comparison has also been performed with a single wavelength which is not corrected for chromatic aberration (see supplementary information, Supplementary Figure S3). The focal length changed by 12% (from 245 μm at 810 nm to 215 μm at 910 nm).

3.4 Metasurfaces for combined performances

Performances were evaluated quantitatively when combing all metasurfaces together. Figure 7A shows the representative cross-sectional views of the electric-field distribution at selected points along the propagation direction. All intensities are normalized to have the same scale bar. The green trail is the beam propagation for the hybrid off-axis focusing metalens at 671 nm excitation. The pink trail is for the beam propagation for the hybrid off-axis focusing metalens at 785 nm excitation. The blue trail is for the achromatic broadband on-axis metalens at 810–910 nm collection. All three metalenses were positioned at $z = 0$. As the beams propagate, the beam profiles converge spatially, and the focal spots coincide at the same focal plane indicated by the black border. Beyond the focal plane, the beams become diverged again. Figure 7B is the 3D perspective view of the beam propagations of the three metalenses. It gives a clear view of the beam profiles at the intersection where the focal plane is. Figure 7C shows the normalized intensity along the x-, y-, and z-axis at the focal plane. The FWHMs were calculated for each metasurface and displayed in the figure. The color code follows that of Figure 7A. By comparing the three FWHMs, the minimum value determines the spatial resolution of the beam profile at the focal plane. In the x- and y-direction, the FWHMs of the combined beam are determined by the collection beam which are both 4.6 μm. In the z-direction, the FWHM of the combined beam is determined by the excitation beam which is 11.3 μm. These values also translate to the effective sensing area on the sample, which is 239.1 μm^3. The achieved spatial resolution is sufficient for common biological applications. Specifically, the spatial resolution in the z-direction is an important parameter for depth information in confocal sensing and imaging. It can be improved by increasing the NA of the metalenses.

4 Conclusion

In this paper, we have proposed an all-metasurface-enabled fiber needle probe for dual-wavelength excitation Raman spectroscopy devices. The new design reduces the overall size by 100 times and improves the optical performance of the existing handheld probe [13]. It consists of five metasurfaces that replace five conventional optical components in the original design. The metasurfaces designed for the excitation fibers at $\lambda = 671\,nm$ and $\lambda = 785\,nm$ include a hybrid configuration of a Fabry-Pérot cavity and a metalens which functions as a narrow band pass filter and an off-axis focusing lens. The total thickness of the hybrid metalens is in the range of 200 nm, not counting the substrate thickness. The metasurface designed for the collection fiber at $\lambda = 810 - 910\,nm$ is an achromatic broadband metalens that functions as an apochromatic objective lens (one of the most expensive objectives) which focuses the incident light at a constant focal length without chromatic and spherical aberration in a broad wavelength range. The total thickness of this metasurface is 1500 nm, not counting the substrate thickness. Our simulation results show that the two incident excitation beams were focused at an angle of 43.4° and −43.4°. The two excitation focal spots and the collection focal spot coincide at the same location on the sample. The profiles of the combined beam were characterized along the x-, y-, and z-axis which correspond to the effective sensing area on the sample of 239.1 μm^3 ($4.6\,\mu m \times 4.6\,\mu m \times 11.3\,\mu m$). All metasurfaces presented here were developed based on state-of-the-art design methodologies and supported by literature for fabricated devices. The parameters of the fiber probes discussed were also based on commercially available fibers, which means the entire proposed design framework can be readily deployed and put into practical use. The new needle probe will enable many new applications using Raman spectroscopy, for example, oral cavity examinations, small animal *in vivo* experiments, endoscopic experiments, and neonatal skin analysis for hard-to-reach areas. Finally, the metasurface design framework can also be generalized to other optical instruments for miniaturization and improved optical performances.

Data availability statement

The raw data supporting the conclusion of this article will be made available by the authors, without undue reservation.

Author contributions

SZ, RB, and RZ conceived the idea. SZ and RS conducted the simulations. SZ, RB, RZ, YQ, and RS analyzed the results. MO supervised the project. SZ and RS drafted the manuscript. All authors reviewed the manuscript.

Funding

Agency for Science Technology and Research Industry Alignment Fund Prepositioning Program (H19H6a0025), Career Development Award (202D800042), and BMRC Central Research Fund Award (CRF, UIBR).

Conflict of interest

The authors declare that the research was conducted in the absence of any commercial or financial relationships that could be construed as a potential conflict of interest.

Publisher's note

All claims expressed in this article are solely those of the authors and do not necessarily represent those of their affiliated organizations, or those of the publisher, the editors and the reviewers. Any product that may be evaluated in this article, or claim that may be made by its manufacturer, is not guaranteed or endorsed by the publisher.

Supplementary material

The Supplementary Material for this article can be found online at: https://www.frontiersin.org/articles/10.3389/fphy.2022.1093284/full#supplementary-material

References

1. Mhlanga N, Tetyana P, Nyembe S, Sikhwivhilu L. Application of Raman spectroscopy in biomedical diagnostics. In: *Recent developments in atomic force microscopy and Raman spectroscopy for materials characterization*. London: IntechOpen (2022).

2. Sato H, Maeda Y, Ishigaki M, Andriana BB. Biomedical applications of Raman spectroscopy. In: *Encyclopedia of analytical chemistry*. John Wiley & Sons (2000). p. 1–12.

3. Choo-Smith LP, Edwards HGM, Endtz HP, Kros JM, Heule F, Barr H, et al. Medical applications of Raman spectroscopy: From proof of principle to clinical implementation. *Biopolymers* (2002) 67:1–9. doi:10.1002/bip.10064

4. Caspers PJ, Lucassen GW, Wolthuis R, Bruining HA, Puppels GJ. *In vitro* and *in vivo* Raman spectroscopy of human skin. *Biospectroscopy* (1998) 4:S31–9. doi:10.1002/(sici)1520-6343(1998)4:5+<s31:aid-bspy4>3.0.co;2-m

5. Pezzotti G, Boffelli M, Miyamori D, Uemura T, Marunaka Y, Zhu W, et al. Raman spectroscopy of human skin: Looking for a quantitative algorithm to reliably estimate human age. *J Biomed Opt* (2015) 20:065008. doi:10.1117/1.jbo.20.6.065008

6. Caspers PJ, Nico C, Bakker Schut TC, Sterke J, Pudney PDA, Curto PR, et al. Method to quantify the *in vivo* skin penetration of topically applied materials based on confocal Raman spectroscopy. *Translational Biophotonics* (2019) 1. doi:10.1002/tbio.201900004

7. Liu K, Zhao Q, Li B, Zhao X. Raman spectroscopy: A novel technology for gastric cancer diagnosis. *Front Bioeng Biotechnol* (2022) 10:856591. doi:10.3389/fbioe.2022.856591

8. Auner GW, Koya SK, Huang C, Broadbent B, Trexler M, Auner Z, et al. Applications of Raman spectroscopy in cancer diagnosis. *Cancer Metastasis Rev* (2018) 37:691–717. doi:10.1007/s10555-018-9770-9

9. D'Acunto M, Gaeta R, Capanna R, Franchi A. Contribution of Raman spectroscopy to diagnosis and grading of chondrogenic tumors. *Sci Rep* (2020) 10:2155. doi:10.1038/s41598-020-58848-0

10. Corden C, Boitor R, Notingher I. Time-gated Raman spectroscopy for biomedical application under ambient or strong background light conditions. *J Phys D: Appl Phys* (2021) 54:504003. doi:10.1088/1361-6463/ac276e

11. Sato H, Shinzawa H, Komachi Y. Fiber-Optic Raman probes for biomedical and pharmaceutical applications. In: Matousek P, Morris MD, editors. *Emerging Raman applications and techniques in biomedical and pharmaceutical fields*. Springer Berlin Heidelberg (2010). p. 25–45.

12. Heng HPS, Shu C, Zheng W, Lin K, Huang Z. Advances in real-time fiber-optic Raman spectroscopy for early cancer diagnosis: Pushing the frontier into clinical endoscopic applications. *Translational Biophotonics* (2021) 3. doi:10.1002/tbio.202000018

13. Zhang R, Bi R, Ho Jun Hui C, Rajarahm P, Dinish US, Olivo M. A portable ultrawideband confocal Raman spectroscopy system with a handheld probe for skin studies. *ACS Sens* (2021) 6:2960–6. doi:10.1021/acssensors.1c00761

14. Katagiri T, Hattori Y, Suzuki T, Matsuura Y, Sato H. Hollow fiber-optic Raman probes for small experimental animals. In: Gannot I, editor. *Optical fibers and sensors for medical diagnostics and treatment applications VII*, 6433 (2007). p. 64330O.

15. Zavaleta CL, Garai E, Liu JTC, Sensarn S, Mandella MJ, Van de Sompel D, et al. A Raman-based endoscopic strategy for multiplexed molecular imaging. *Proc Natl Acad Sci U S A* (2013) 110:E2288–97. doi:10.1073/pnas.1211309110

16. Trägårdh J, Pikálek T, Šerý M, Meyer T, Popp J, Čižmár T. Label-free CARS microscopy through a multimode fiber endoscope. *Opt Express* (2019) 27:30055. doi:10.1364/oe.27.030055

17. Yu X, Zhang S, Olivo M, Li N. Micro- and nano-fiber probes for optical sensing, imaging, and stimulation in biomedical applications. *Photon Res* (2020) 8:1703. doi:10.1364/prj.387076

18. Yu N, Genevet P, Kats MA, Aieta F, Tetienne J-P, Capasso F, et al. Light propagation with phase discontinuities: Generalized laws of reflection and refraction. *Science* (2011) 334:333–7. doi:10.1126/science.1210713

19. Chen WT, Zhu AY, Capasso F. Flat optics with dispersion-engineered metasurfaces. *Nat Rev Mater* (2020) 5:604–20. doi:10.1038/s41578-020-0203-3

20. Arbabi A, Horie Y, Ball AJ, Bagheri M, Faraon A. Subwavelength-thick lenses with high numerical apertures and large efficiency based on high-contrast transmitarrays. *Nat Commun* (2015) 6:7069. doi:10.1038/ncomms8069

21. Park J-S, Zhang S, She A, Chen W-T, Yousef KMA, Capasso F, "Large-area, single material metalens in the visible: An approach for mass-production using conventional semiconductor manufacturing techniques," in *Optics InfoBase conference papers* (2019), Vol. Part F129.

22. She A, Zhang S, Shian S, Clarke DR, Capasso F. Large area metalenses: Design, characterization, and mass manufacturing. *Opt Express* (2018) 26:1573. doi:10.1364/oe.26.001573

23. Zhang S, Soibel A, Keo SASA, Wilson D, Rafol SBSB, Ting DZDZ, et al. Solid-immersion metalenses for infrared focal plane arrays. *Appl Phys Lett* (2018) 113:111104. doi:10.1063/1.5040395

24. Zhu AY, Kuznetsov AI, Luk'yanchuk B, Engheta N, Genevet P. Traditional and emerging materials for optical metasurfaces. *Nanophotonics* (2017) 6:452–71. doi:10.1515/nanoph-2016-0032

25. Jung C, Kim G, Jeong M, Jang J, Dong Z, Badloe T, et al. Metasurface-driven optically variable devices. *Chem Rev* (2021) 121:13013–50. doi:10.1021/acs.chemrev.1c00294

26. Zhang C, Divitt S, Fan Q, Zhu W, Agrawal A, Lu Y, et al. Low-loss metasurface optics down to the deep ultraviolet region. *Light Sci Appl* (2020) 9:55. doi:10.1038/s41377-020-0287-y

27. Zhang S, Wong CL, Zeng S, Bi R, Tai K, Dholakia K, et al. Metasurfaces for biomedical applications: Imaging and sensing from a nanophotonics perspective. *Nanophotonics* (2020) 10:259–93. doi:10.1515/nanoph-2020-0373

28. Li Z, Tian X, Qiu C-W, Ho JS. Metasurfaces for bioelectronics and healthcare. *Nat Electron* (2021) 4:382–91. doi:10.1038/s41928-021-00589-7

29. Pahlevaninezhad M, Huang YW, Pahlevani M, Bouma B, Suter MJ, Capasso F, et al. Metasurface-based bijective illumination collection imaging provides high-resolution tomography in three dimensions. *Nat Photon* (2022) 16:203–11. doi:10.1038/s41566-022-00956-6

30. Chen WT, Zhu AY, Sanjeev V, Khorasaninejad M, Shi Z, Lee E, et al. A broadband achromatic metalens for focusing and imaging in the visible. *Nat Nanotech* (2018) 13:220–6. doi:10.1038/s41565-017-0034-6

31. Wang Y, Chen Q, Yang W, Ji Z, Jin L, Ma X, et al. High-efficiency broadband achromatic metalens for near-IR biological imaging window. *Nat Commun* (2021) 12:5560. doi:10.1038/s41467-021-25797-9

32. Ramakrishnaiah R, ur Rehman G, Basavarajappa S, Al Khuraif AA, Durgesh BH, Khan AS, et al. Applications of Raman spectroscopy in dentistry: Analysis of tooth structure. *Appl Spectrosc Rev* (2015) 50:332–50. doi:10.1080/05704928.2014.986734

33. Cordero E. *In-vivo* Raman spectroscopy: From basics to applications. *J Biomed Opt* (2018) 23:1. doi:10.1117/1.jbo.23.7.071210

34. Stamatas GN, Nikolovski J, Mack MC, Kollias N. Infant skin physiology and development during the first years of life: A review of recent findings based on *in vivo* studies. *Int J Cosmet Sci* (2011) 33:17–24. doi:10.1111/j.1468-2494.2010.00611.x

35. Benoît A, Dauliat R, Jamier R, Humbert G, Grimm S, Schuster K, et al. Highly efficient higher-order modes filtering into aperiodic very large mode area fibers for single-mode propagation. *Opt Lett* (2014) 39:4561. doi:10.1364/ol.39.004561

36. Wang Y, Zhu X, Chen Y, Shi H, Li Z, Zhang S, et al. Fabrication of Fabry–Perot-cavity-based monolithic full-color filter arrays using a template-confined micro-reflow process. *J Micromech Microeng* (2019) 29:025008. doi:10.1088/1361-6439/aaf6cb

37. Khorasaninejad M, Chen WT, Oh J, Capasso F. Super-dispersive off-Axis meta-lenses for compact high resolution spectroscopy. *Nano Lett* (2016) 16:3732–7. doi:10.1021/acs.nanolett.6b01097